ELSEVIER

Surface Science 444 (2000) 31–51

surface science

www.elsevier.nl/locate/susc

The prediction of metastable impact electronic spectra (MIES): perfect and defective MgO(001) surfaces by state-of-the-art methods

L.N. Kantorovich [a], A.L. Shluger [a,*], P.V. Sushko [a,b], A.M. Stoneham [a]

[a] *Department of Physics & Astronomy, University College London, Gower Street, London WC1E 6BT, UK*
[b] *The Royal Institution of Great Britain, 21 Albemarle Street, London W1X 4BS, UK*

Received 26 May 1999; accepted for publication 30 September 1999

Abstract

surfaces. This suggests a quantitative approach which takes advantage of recent developments in highly efficient many-electron computational techniques. It gives a basis to the interpretation of experimental MIES spectra for perfect and defective surfaces. Our method is based on a static approach to predicting Auger de-excitation (AD) rates of $He^*(1s2s)$ projectiles. A key quantity is the surface density of states (DOS) projected on the 1s orbital of the He^* atom, which is calculated along its trajectory. We use density functional theory within both supercell geometry and embedded cluster models to calculate MIES spectra for the perfect MgO surface and for an MgO surface with different concentrations of adsorbed oxygen atoms. First we calculate the Auger de-excitation rates at various positions of the projectile above the surface. To predict MIES spectra, we integrate over projectile trajectories, with a subsequent weighted averaging with respect to various lateral positions of He^* above the MgO surface unit cell. It is important to examine final-state effects for a correct comparison between theory and experiment, especially when there are localised defect states.

Keywords: Adatoms; Atom–solid interactions; Auger ejection; Density functional calculations; Electron emission; Magnesium oxides; Metastable induced electron spectroscopy; Surface defects

1. Introduction

When a slow, electronically excited rare gas atom impinges on a solid surface, its excitation energy can be transferred to kinetic energy of an ejected electron. These measured kinetic energy spectra contain information about electronic processes taking place during impact of the excited particle with the surface. The experimental technique based on this effect is known as metastable impact electron spectroscopy (MIES) or metastable atom electron spectroscopy (MAES). The several different processes leading to electron ejection have been considered in Ref. [1]. Extensive applications of this technique to study metal surfaces have recently been reviewed in Ref. [2]. However, there have been few applications of MIES to insulating surfaces until recently, partly because of the complications of surface charging. Yet there is strong interest in thin oxide films on metals, and

* Corresponding author. Fax: +44-171-391-1360.
E-mail address: a.shluger@ucl.ac.uk (A.L. Shluger)

0039-6028/00/$ - see front matter
PII: S0039-6028(99)01049-3

advances in the controlled growth of such films has prompted increasing applications of MIES to insulators, as reviewed in Ref. [3]. So far, the interpretation of MIES spectra has been based on intuitive models [4–6]. We shall re-examine these ideas so that we can apply state-of-the-art methods to perfect surfaces, and also show how surface defects modify MIES spectra. This paper concentrates on one of the most common MIES situations, in which metastable excited helium atoms, $He^*(1s2s)$, approach an insulating surface with thermal velocities. In many experiments (see below) the informative part of the MIES spectra on insulators comes from the so-called Auger de-excitation (AD) process. In this process, a surface electron tunnels into the singly-occupied 1s state of the He^* atom, with simultaneous ejection of the excited He(2s) electron. The focus of this paper is on the distribution of kinetic energies of these ejected electrons.

The theory of AD processes for metal surfaces has been discussed in detail in the literature. In particular, Hagstrum [1] suggested a theory based on standard perturbation theory (Fermi's Golden rule) and one-electron wavefunctions. His so-called *static* approach recognised the valuable assumption that the projectile could be assumed to be fixed at some position $\boldsymbol{R}$ along its path $\boldsymbol{R}(t)$ above the surface. The transition rate (per unit time), $\Re(\boldsymbol{R})$, can then be calculated for the process to happen during the next instant $\mathrm{d}t$. The distance moved in this interval is $\mathrm{d}R = v_0\,\mathrm{d}t$, where v_0 is the projectile velocity. The total probability $P(\boldsymbol{R})\,\mathrm{d}t = P(\boldsymbol{R})|\mathrm{d}R/v_0|$ for the transition to happen in the time for the projectile to move from $\boldsymbol{R}$ to $\boldsymbol{R}+\mathrm{d}\boldsymbol{R}$ is given as a product of $\Re(\boldsymbol{R})\mathrm{d}t$ and the so-called escape probability,

$$P_{\mathrm{esc}}(\boldsymbol{R}) = \exp\left(-\int_{\boldsymbol{R}}^{\infty} \Re(\boldsymbol{R}') \left| \frac{\mathrm{d}\boldsymbol{R}'}{v_0} \right| \right), \qquad (1)$$

which is the probability for the transition *not to happen* along the incoming part of the trajectory from infinity to $\boldsymbol{R}$. Multiple exchanges of electrons are not included. One expects the rate $\Re(\boldsymbol{R}) \propto \exp(-\alpha z)$ to fall off exponentially because of the decay of the surface wavefunctions into the vacuum (the z axis is the normal to the surface directed into the vacuum). Simple arguments suggest then that the total probability, $P(\boldsymbol{R})$, will be peaked at a distance R_{mp} from the surface of the order of several Å. For an atom with a linear incident trajectory of constant velocity, the probability for the transition to occur anywhere on the *incoming* part of the trajectory is given by the integral $\int_0^{\infty} P(\boldsymbol{R})|\mathrm{d}R/v_0| = 1 - \exp[-\exp(\alpha R_{\mathrm{mp}})]$. In most cases, this has a value very close to unity [1,7], since $\alpha R_{\mathrm{mp}} \gg 1$. Static calculations of the Auger processes based on Fermi Golden rule expressions for the transition probability have been given, for example, in Refs. [8–13].

Significant progress has been achieved in *dynamic* calculations of Auger processes using a variety of methods. Thus, in Refs. [14–17], the time-dependent Schroedinger equation is solved in a space spanned by a limited set of Slater determinants, ψ_a, related to the processes of interest. The full Hamiltonian $\hat{H}(t)$ used includes the atom (ion)–surface interaction term explicitly [time dependence enters via the projectile position $\boldsymbol{R}(t)$ above the surface]; the *evolution* of the wavefunction $\Psi(t) = \sum_a C_a(t)\psi_a$ of the *combined* system is calculated. The probability for reaching a chosen final state ψ_{f} after Auger de-excitation is then $P_{\mathrm{f}} = |\langle\psi_{\mathrm{f}}|\Psi(\infty)\rangle|^2$ by standard quantum mechanics. Physically equivalent but mathematically distinct methods are used by some other workers. In Refs. [18,19] the time evolution of the combined system is studied using the Keldysh Green's function formalism [20] for time-dependent Hamiltonian operators. Moyer and Orvek [21, 22] base a general theory on the equation of motion for the evolution operator $U(t, -\infty) = \langle\Psi(t)|\Psi(-\infty)\rangle$, and apply it to the neutralisation of slowly moving ions at metal surfaces. They find that, for ions with energies above 2 eV, or at very short ion–surface distances (around several Å), the transition probability may have a complex oscillatory behaviour. However, the transition probabilities for slow energy particles, interacting weakly with the surface, are found to agree well with predictions from the Fermi Golden rule expression smeared out by a Lorentzian due to dynamical effects.

Although the basic mechanisms of the AD process are reasonably well understood, it has not

proved simple to apply existing theories to the interpretation of experimental data. What is needed is a combination of the AD theory and the electronic structure of realistic systems, including surface defects and adsorbed species. Such electronic structure calculations are still complex and time-consuming. In many cases, especially for insulating surfaces, attempts to model MIES spectra use simple or intuitive models. In Refs. [4,6,23] it is assumed that the main transition mechanism is Auger de-excitation, and the MIES spectra have been simulated by the surface density of states (DOS) projected on the surface oxygen ions of the uppermost surface layer using a Hartree–Fock method (the CRYSTAL code [24,25]) and a density functional theory (DFT) method (the CETEP code [26]). The effect of the overlap between the surface and He(1s) wavefunctions was taken into account only approximately by applying an additional z-dependent exponential factor to the surface DOS. Other workers [5,6] estimated the AD transition probability using a DOS projected on to the projectile 1s atomic orbital. However, they were not able to use state-of-the-art methods for the surface electronic structure. Yet the success of the simplified treatments [4–6], especially for MIES features such as relative energies of the different peaks, suggests that real spectra are indeed related to the projection of the surface DOS on to the projectile orbital.

In this paper, we take the next step. We attempt to calculate MIES spectra for typical cases using both AD theory and density functional theory of the surface electronic structure. We demonstrate how, by using a number of approximations, one can obtain an expression for the MIES spectrum which indeed appears to be proportional to the projected surface DOS. A complete approach includes also a detailed study of the dependence of AD transition rate on the position of He^* with respect to the surface. One must average over positions, and integrate over the projectile trajectory. The MIES spectrum of the perfect MgO surface that we predict is close in many ways to the experimental one reported in Ref. [4]. The differences between our theory and experiment point to further challenges, which we discuss.

A second major issue which we address relates to the effect of *surface defects* on the spectra obtained by ultraviolet photoemission spectroscopy (UPS) and MIES. Can our theory predict particular '*signatures*' in the MIES spectrum to aid defect recognition in experiments? Comparison with experiment needs both estimates of defect concentrations on the surface and also the possibility of different defect *orientations*. An important point concerns the energies of local defect states with respect to the oxygen O(2p) band observed in UPS and MIES spectra, and their interpretation. We shall argue that the defect-related features in MIES spectra can be significantly *shifted* with respect to those in projected DOS due to final-state effects; i.e., crystal electronic polarisation due to the hole localisation on the defect after electron tunnelling to He^* in the AD process. We have chosen as a representative defect one which has already been analysed in some detail in Refs. [27–29]; namely, an oxygen atom adsorbed on the MgO(001) surface.

The paper is organised as follows. In Section 2 we briefly review the theory of AD processes for a slowly moving metastable atom (such as He^*) incident on an insulating surface. This analysis leads to a simple expression for the AD transition rate based on the DOS projected on the $He^*(1s)$ orbital. We also discuss the final-state effects (crystal polarisation due to hole formation in the crystal) and the physical effects which may lead to the broadening of the calculated spectra. Details of the electronic structure methods used are also given in Section 2. The results of our calculations of the MIES spectra for perfect and defective surfaces are presented in Section 3; our discussions and conclusions are given in Section 4.

2. Theory

2.1. Calculation of the transition rate

The interpretation of MIES experiments follows the model of Refs. [1,30,31] shown in Fig. 1. Excited helium atoms (atomic state 1s2s) approach a surface with thermal velocities at an incidence angle of 45°. Their triplet/singlet ($2^3S/2^1S$) ratio is about 7:1 in real experiments [4]. For many

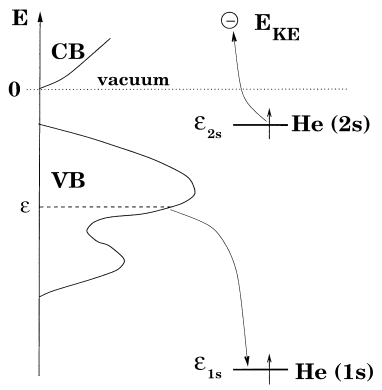

Fig. 1. Schematic representation of the Auger de-excitation process. The helium atom enters in an excited (1s, 2s) triplet state and leaves in its ground singlet state.

insulators, the top of the valence band with respect to the vacuum is much lower than the ionisation potential of He*. In such cases, only AD processes are important. The static approach should apply, since He* atoms have only thermal velocities, and interact only weakly with most such surfaces.

We shall need a working model. Let us consider a *triplet* He* atom at position $\boldsymbol{R}=(x, y, z)$ above the surface. In the initial state (before the transition; we use index i), we have the He* atom and the ground-state crystal surface. In the final state (index f), there is a hole with spin down in state k (with the energy $-\epsilon_k$) and a free electron with spin up, momentum $\boldsymbol{Q}$ and energy $E_{\mathrm{KE}}(\boldsymbol{Q})\simeq(\hbar^2/2m)\boldsymbol{Q}^2$; the helium atom is now in its ground (singlet) state. The total energies of the whole system in the initial and final states are:

$$E_{\mathrm{i}}=E_0+E_{\mathrm{He*}} \tag{2}$$

and

$$E_{\mathrm{f}}^{(k\boldsymbol{Q})}=E_{\mathrm{h}}^{(k)}+E_{\mathrm{He}}+E_{\mathrm{KE}}(\boldsymbol{Q}), \tag{3}$$

where E_0 is the energy of the crystal prior to the transition and $E_{\mathrm{h}}^{(k)}$ is its energy with one hole in state $(k\downarrow)$. We use standard quantum methods to calculate the transition rate in the *static* approximation already described. The interaction between the crystal and the He* atom, $\hat{H}_{\mathrm{int}}$, depends explicitly on the actual position $\boldsymbol{R}$ of the helium atom above the surface. The energies E_{i} and $E_{\mathrm{f}}^{(k\mathbf{Q})}$ in Eqs. (2) and (3), respectively, correspond to the Hamiltonian without interaction and therefore do not depend on $\boldsymbol{R}$.

The transition probability per unit time to emit an electron with momentum $\boldsymbol{Q}$ is:

$$\Re(\boldsymbol{Q})=\frac{2\pi}{\hbar}\sum_{k}^{\mathrm{occ}}|W_{k\boldsymbol{Q}}|^2\delta(E_{\mathrm{i}}-E_{\mathrm{f}}^{(k\boldsymbol{Q})}). \tag{4}$$

We sum over all occupied states of the crystal. The perturbation matrix element is given as [1,2]:

$$W_{k\boldsymbol{Q}}=\int\frac{\mathrm{d}\boldsymbol{r}_1\mathrm{d}\boldsymbol{r}_2}{|\boldsymbol{r}_1-\boldsymbol{r}_2|}\psi_{1\mathrm{s}}(\boldsymbol{r}_1)\psi_k(\boldsymbol{r}_1)\psi_{2\mathrm{s}}(\boldsymbol{r}_2)\psi_{\boldsymbol{Q}}(\boldsymbol{r}_2). \tag{5}$$

This expression is valid in the Hartree–Fock approximation; the system has *triplet* spin symmetry in both initial and final states. In the case of the *singlet* He* atom, where the final state will preserve the spin symmetry, there is an additional term which disappears in the triplet state through integration over spins (see, for example, Ref. [2]). In the final state, the crystal will be polarised by the hole created on emission of the electron. We assume, however, that this effect on the electronic *wavefunctions* is insignificant and neglect it in this study.

The double-space integral in Eq. (5) is very difficult to calculate using the ab initio wavefunctions ψ_k specified on the real-space grid, as in most conventional plane-wave DFT calculations and including those used in our work. However, we can simplify the expression using the following argument. The integral in Eq. (5) can be interpreted as the matrix element $\langle\psi_{1\mathrm{s}}(\boldsymbol{r}_1)|V_{\boldsymbol{Q},2\mathrm{s}}(\boldsymbol{r}_1)|\psi_k(\boldsymbol{r}_1)\rangle$ of the Coulomb potential, $V_{\boldsymbol{Q},2\mathrm{s}}(\boldsymbol{r}_1)$, arising from the charge density $\psi_{2\mathrm{s}}(\boldsymbol{r}_2)\psi_{\boldsymbol{Q}}(\boldsymbol{r}_2)$. Our Hartree–Fock calculations of the triplet He* atom show that the He(2s) orbital is very diffuse (its radius is $\simeq$2.26 Å); the He(1s) orbital is much more localised (its radius is $\simeq$0.40 Å). Given this, and the fact that the orbital $\psi_{\boldsymbol{Q}}(\boldsymbol{r}_2)$ is a plane wave, one can expect that the potential $V_{\boldsymbol{Q},2\mathrm{s}}(\boldsymbol{r}_1)$ varies only slowly in space. If it is sensibly constant within the area of significant overlap between the functions $\psi_{1\mathrm{s}}$ and ψ_k, then we may simplify the integral by taking the potential out of the matrix element. The simplified integral is proportional to an over-

lap integral $\langle\psi_{1s}(r_1)|\psi_k(r_1)\rangle$. The obvious gain is that, instead of the rather complicated double-space integral of Eq. (5), we have an overlap integral which can be easily calculated on a real-space grid. Turning to the transition rate of Eq. (4), we have now:

$$\Re(\boldsymbol{Q}) \propto \left[\sum_k^{\text{occ}} |\langle\psi_k|\psi_{1s}\rangle|^2 \delta(E_i - E_f^{(k\boldsymbol{Q})}) \right]. \tag{6}$$

The expression in square brackets proves to be proportional to the crystal DOS *projected* on the He(1s) orbital. The energy in the δ-function can be expressed in terms of one-electron energies ϵ_k of the crystal orbitals ψ_k. We adopt the following *definition*:

$$E_h^{(k)} = E_0 - \epsilon_k + W_{\text{pol}}^{(k)}. \tag{7}$$

Here, $W_{\text{pol}}^{(k)}$ accounts for all electron relaxation and correlation effects on forming the electron hole in the AD process. This relaxation energy can be calculated using simple models (e.g., Ref. [32]). Using Eqs. (2), (3) and (7) in Eq. (6), we finally obtain:

$$\Re(E_{\text{KE}}, \boldsymbol{R}) = C \cdot D_{1s}(E_{\text{KE}} + W_{\text{pol}}^{(k)} + E_{\text{He}} - E_{\text{He}^*}, \boldsymbol{R}), \tag{8}$$

where C is a proportionality factor which we assume is the same for perfect and defective surfaces. It will be discussed in a later section. This expression shows explicitly the dependence on the position of the helium atom and on the kinetic energy of the emitted electron. The quantity

$$D_{1s}(E, \boldsymbol{R}) = \sum_k^{\text{occ}} |\langle\psi_k|\psi_{1s}\rangle|^2 \delta(E - \epsilon_k) \tag{9}$$

introduced in Eq. (8) is the crystal DOS *projected* on the 1s orbital of the helium atom and calculated at the energy $E = E_{\text{KE}} + W_{\text{pol}}^{(k)} + E_{\text{He}} - E_{\text{He}^*}$. The projected DOS can be calculated routinely with modern ab initio methods. For delocalised hole states $W_{\text{pol}}^{(k)} \simeq 0$. However, $W_{\text{pol}}^{(k)}$ can be significant if an AD process creates a hole in a localised defect state; this we shall refer to as the *final-state* effect.

Eq. (8) allows one to calculate the probability (per unit time) of an AD process in which a free electron of energy $E_{\text{KE}} \simeq (\hbar^2/2m)\boldsymbol{Q}^2$ and momentum $\boldsymbol{Q}$ is emitted. The projected DOS has also been used by other authors (see, e.g., Refs. [4,5,30,31]), but without detailed justification. A more general derivation of this result is given in the Appendix. We are also aware of other routes to the same result, based on more conventional approaches to Auger transitions [33].

2.2. Calculation of MIES spectra

Our aim is to calculate a spectrum that can be compared directly with experiment. This means we must consider the trajectory of the incident helium atom. In particular, one has to multiply the transition probability $\Re(E_{\text{KE}}, \boldsymbol{R})$ by the probability that there has been no earlier transition, using the escape probability of Eq. (1), where

$$\Re(\boldsymbol{R}) = \int \Re(E_{\text{KE}}, \boldsymbol{R})\, \mathrm{d}E_{\text{KE}} \tag{10}$$

in Eq. (1) is the total probability to emit an electron with any energy during the time $\mathrm{d}t$ between $\boldsymbol{R}$ and $\boldsymbol{R} + \mathrm{d}\boldsymbol{R}$ along the trajectory. One must sum over all possible *events*, i.e., consider transitions at all times t along the *same* trajectory, which turns into an integral over the whole incoming *trajectory* of the projectile. The total spectrum requires an *ensemble average* $\langle\ldots\rangle$ over the different starting positions of the helium atoms with respect to the surface unit cell, i.e., with respect to all possible trajectories:

$$P(E_{\text{KE}}) = \left\langle \int \Re(E_{\text{KE}}, \boldsymbol{R}_t) P_{\text{esc}}(\boldsymbol{R}_t)\, \mathrm{d}t \right\rangle, \tag{11}$$

where $\boldsymbol{R}_t$ indicates explicitly the time dependence of $\boldsymbol{R}$. This general expression can be used for any trajectories of He^* atoms, provided there are no multiple transitions.

We shall concentrate on a simplified model in which all the trajectories are assumed to be perpendicular to the surface. In this case, the integral over the trajectory is an integral over z, and the averaging with respect to starting lateral positions of helium atoms at infinity is equivalent to averaging over various positions of the projectile in the x, y plane.

As noted in the Introduction, the exponential decay of the crystal wavefunctions suggests that

the rate $\Re(E_{KE}, \boldsymbol{R})$ should decay exponentially with increasing distance z from the surface. The characteristic decay length will depend on energy E_{KE}; i.e., $\Re(E_{KE}, \boldsymbol{R}) \propto \exp[-\alpha(E_{KE})z]$. In the next section, we show that the exponentials $\alpha(E_{KE})$ are of the order of several inverse Å, and also depend on which part of the surface unit cell the projectile impinges. The escape probability has the opposite behaviour, being unity at large z and close to zero for small z. The integrand in Eq. (11) will be peaked therefore at some $R_{mp}(E_{KE})$. The peak is not sharp, so, in effect, the integration in Eq. (11) will lead to some *broadening* of the transition probability $\Re(E_{KE}, \boldsymbol{R}_{mp})$ from the value predicted solely at the most probable target distance R_{mp}. In this paper we use the model suggested by Hagstrum [1] to calculate the whole contribution over the projectile trajectory numerically. The final spectrum $P(E_{KE})$ is then obtained by averaging with respect to different positions at which the helium atom impinges on the surface. We shall discuss how this is done in practice in Section 3.

We note in passing that in the kinetic model suggested in Refs. [30,31] and applied to MgO in Ref. [4], the problem with integration over the trajectory does not appear at all. In fact, the problem is hidden in the time-dependence of the helium atom concentrations $N[\mathrm{He}^*]$ and $N[\mathrm{He}]$. The transition rate $\Re(E_{KE}, \boldsymbol{R})$ can be used directly as the input. However, we shall not pursue this method here.

An important issue concerns spectral broadening. Dynamical calculations of the atomic collisions with metal surfaces (see, e.g., Refs. [21,22]) show that the δ-function which appears in the transition rate formula above should be replaced by a Lorentzian. The appropriate breadth depends on the speed of the helium atom, its distance to the surface, and the interaction potential. This leads to a *broadening* of spectra calculated in any static approach. This motional broadening is accompanied by lifetime broadening of the incoming atom [22]. There is also phonon broadening (see Refs. [32–36]), which is well described by a Gaussian of width which depends on temperature. We shall take these effects into account phenomenologically by smearing out the calculated spectra with a Gaussian of dispersion 0.5 eV. This value has been estimated in Ref. [4] using a simple model due to Ref. [36]. We have also run selected calculations with the dispersion 0.8 eV, discussed later.

2.3. Details of the calculation

We shall use two approaches within the widely used density functional theory [37] (for its applications to oxide surfaces see, e.g., Ref. [38]). For the calculations of the final-state effects, which essentially require calculations of ionisation energies, we adopt an *embedded cluster* model [39,40]. To model the MIES spectra, we calculated the projected DOS using a *periodic model* and plane wave basis set. This method has already been used to study the MgO(001) surface [41] and adsorption on it of atomic [27–29] and molecular [28,29] oxygen.

In the embedded cluster calculations, quantum mechanical (QM) clusters of up to 35 atoms were treated using the DFT. Fig. 2 shows the largest QM cluster, $Mg_{25}O_{10}$, which also includes an adsorbed oxygen atom. It was embedded in a finite cluster (region I) of $12 \times 12 \times 6$ ions treated in a polarisable ion model. Pair potentials [42] were used to calculate the interactions between these ions, and the shell model [43] to treat the polarisable oxygen ions. The QM cluster and region I were embedded into an outer region of frozen ions, which make the total number of ions in the system $20 \times 20 \times 8$. The effective charges on all classical ions were $\pm 2e$ (where e is the electron charge). This formulation provides correct values of the

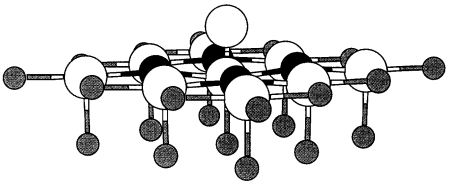

Fig. 2. The quantum cluster $Mg_{25}O_{10}$ containing an adsorbed oxygen atom in the upright position above the central surface oxygen ion. Oxygen ions are represented by white circles, magnesium ions by black circles. The magnesium ions shown in grey carry full-ionic pseudopotentials and one 1s orbital, as described in the text. The cluster shown is embedded into a finite array of polarisable ions surrounded by a finite array of point charges (not shown).

Madelung potential and its gradients on the ions in region I and in the QM cluster.

The matrix elements of the electrostatic potential of the rest of the system, including the dipole contributions from the polarised oxygen ions in region I, are included in the Kohn–Sham equations implemented in the modified GAUSSIAN94 code [44]. The B3LYP functional [45] was employed to calculate the electronic structure of QM clusters. All electrons of oxygen ions (shown in white in Fig. 2) as well as of magnesium ions (shown in black) were described using the 6-31G standard Gaussian basis set [46]. To facilitate calculations of large QM clusters, the magnesium ions shown as grey in Fig. 2 were treated using the pseudopotentials of Wadt and Hay [47] and a 1s function described by two contracted Gaussians. For all clusters considered, magnesium atoms that had less than three nearest quantum oxygens were treated in the similar way.

The periodic DFT method we use is largely the same as that of Refs. [27–29,39–41], except that here we use the local density approximation (LDA) [48]. The calculations of the wavefunctions ψ_k and band energies ϵ_k were performed using the CASTEP code [37]. The cell sizes, the vacuum widths and the system geometries are the same as in our previous study on peroxides [27–29]. In all our calculations the interionic distance of $d_0 = 2.122$ Å has been used to specify the surface unit cells. The projected DOS of Eq. (9) was calculated using the method of tetrahedra as outlined in Ref. [41]. First, the mesh of $\boldsymbol{k}$-points needed was generated using the point-group symmetry of the cell. Then the wavefunctions and energies of the surface electrons were calculated using the CASTEP code for all non-equivalent $\boldsymbol{k}$-points.

To calculate the projected DOS, we need to know the 1s wavefunction of the He^* atom. We have used a linear combination of s-type Gaussian atomic orbitals centred on the helium atom in an ab initio Hartree–Fock calculation of the He^* atom using the GAUSSIAN94 code. The latter calculation has been performed using an sp basis set derived from the standard cc-pVQZ basis set [44] and extended by adding four s and three p diffuse orbitals. For the range of distances z above the surface used in this study (see the next section), we find that the 1s wavefunction depends very little on the actual position of the helium atom above the surface unit cell (on x, y) as well as on z. This allows us to use the wavefunction calculated for the free He^* atom. The overlap integral between the crystalline and He(1s) wavefunctions was calculated numerically on the real-space grid. The results of the calculations were analysed and the projected DOS calculated using the general visualisation program LEV00 [49].

3. Results

3.1. Perfect MgO(001) surface

In studying the perfect MgO(001) surface, we use a four-layer slab with a unit cell containing 32 atoms. There are four magnesium and four oxygen atoms in each layer, and the width is equivalent to four atomic layers. A similar system was considered in Ref. [27], and we use the ionic geometry obtained there. The $\boldsymbol{k}$-points that are not equivalent by symmetry are identified by using the D_{4h} point group. We use 10 $\boldsymbol{k}$-points to obtain the projected DOS and to calculate the transition rate with Eqs. (8) and (9); these points correspond to 2058 tetrahedra in the Brillouin zone. The final smeared DOS is not very sensitive to the number of $\boldsymbol{k}$-points used.

The projected DOS has been calculated for a number of z values between 1 and 4 Å at the four positions of the projectile above the surface unit cell shown in Fig. 3a. The maximum value of z is limited to $\simeq 5$ Å, which is half of the vacuum width used in the electronic structure calculations

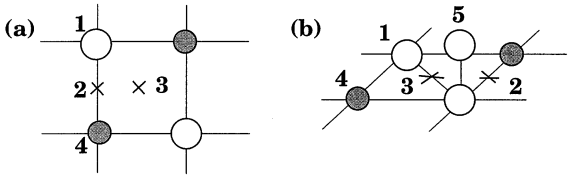

Fig. 3. Positions of the He^* atom: (a) above the (001) MgO surface for the perfect surface and (b) above the upright peroxide molecule. The positions above the interstitial sites which we treat are shown by crosses.

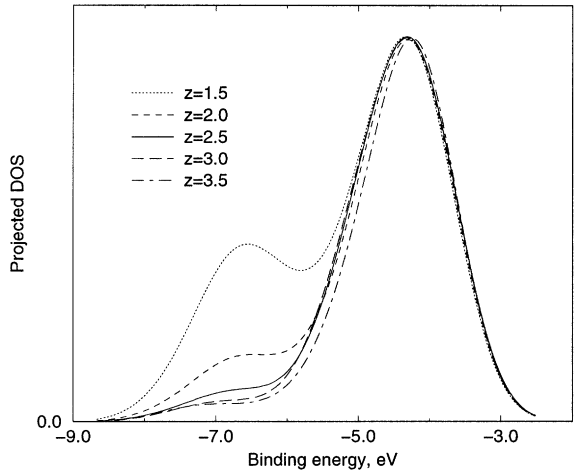

Fig. 4. Projected DOS calculated for different heights z of the helium atom above surface oxygen. The curves are normalised to the same intensity of the right-hand peak, which corresponds to lower binding energies and a smaller inverse decay length.

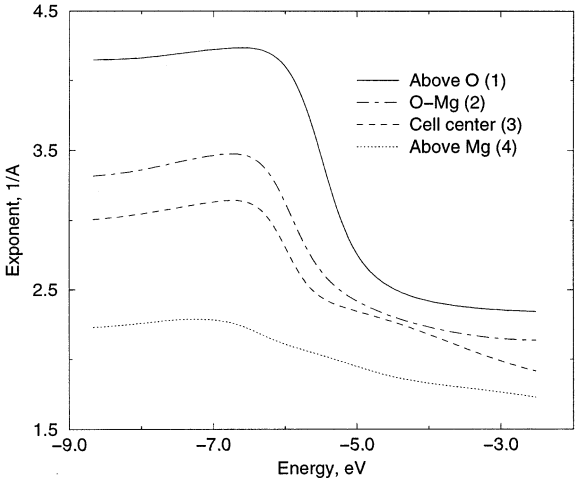

Fig. 5. The exponent $\alpha(E)$ as a function of binding energy E (see text) for the four positions of the helium atom above the surface primitive unit cell. Numbers in brackets correspond to the four positions shown in Fig. 3a.

in the slab model. The four lateral positions are: (1) above the surface oxygen; (2) midway between oxygen and magnesium ions (side); (3) above the centre of the cell (centre); and, finally, (4) above the surface magnesium ion. As expected, we found that the dependence of the projected DOS $D_{1s}(E, z)$ on z changes with energy. This is shown in Fig. 4 for the helium atom above the oxygen site; for ease of comparison, the curves have been normalised to the same intensity of the right-hand peak. Similar results are obtained above the other three sites depicted in Fig. 3a. The intensity of the left-hand (high binding energy) peak decays much faster than the right-hand (low binding energy) peak for z values above $\simeq 2.5$ Å. This is because states with higher binding energies decay more rapidly into the vacuum. For the same reason, the left-hand (higher binding energy) shoulder of the main peak moves to the right (towards lower binding energies). In our previous study in Ref. [4] we found that this holds approximately for the Kohn–Sham orbitals calculated in the slab model between $z \simeq 2$ Å and the middle of the vacuum width. We also showed that the corresponding exponentials are proportional to the square root of binding energies associated with the orbitals ψ_k, as it should be [50,51].

Fig. 4 emphasises the changes in shape of the predicted DOS with z by showing curves normalised to highlight the approximate constancy of shape of the low-binding-energy peak. Clearly, it is important to consider the integrated area $D(z) = \int D_{1s}(E, z)\, dE$ under each curve, which should decay with z as well. We show this for the four sites of Fig. 3a. For each site, and for *every* energy E, we can fit the calculated projected DOS $D_{1s}(E, z)$ to an exponential form $\exp[-\alpha(E)z]$. The inverse decay lengths $\alpha(E)$ are plotted in Fig. 5. These curves have two reasonably flat regions, separated by a region in which $\alpha(E)$ changes rapidly. The flat regions show that the inverse decay length $\alpha(E)$ is almost constant across each of the two peaks in the DOS (one peak corresponds to binding energies between 6 and 8 eV; the other peak corresponds to binding energies between about 3 and 4.5 eV). The inverse decay lengths are very different for the two peaks; they also depend strongly on the lateral position of the helium atom above the surface.

To summarise, $\alpha(E)$ is roughly constant over the high-binding-energy peak, and corresponds to a rapid decay into the vacuum. Over the low-binding-energy peak, $\alpha(E)$ is again roughly constant, but smaller, so that decay is slower. The

results also show that decay is much slower above magnesium and much faster above oxygen. Values for the two interstitial sites are intermediate, and similar in value to each other.

We need to integrate the transition probability along the trajectory of the projectile, and then average the results over the lateral positions. For projectiles approaching the surface along the normal with constant velocity v_0, the integral over time t in Eq. (11) can be replaced by an integral over z divided by the velocity. In addition, the integration with respect to the trajectory in Eq. (1), which defines the escape probability, can also be replaced by dz'/v_0. Then, in order to calculate the integral over dz'/v_0 in Eq. (1) for the escape probability, one has to have a simple and accurate expression for the total probability $\Re(z)=C\cdot D(z)$ as a function of z, where $D(z)$ is the total *area* under each projected DOS [cf. Eqs. (8) and (10)]. We find that $D(z)$ can be approximated quite well by a single exponential, $D(z)\simeq\zeta\cdot\exp(-\alpha z)$, which results in a simple expression for the escape probability (see below). The exponents α for the four sites of Fig. 3a are, respectively, 3.25, 2.42, 2.24 and 1.78 Å^{-1}. These energy-averaged values show the same trends as the curves in Fig. 5. The main contribution to these inverse decay lengths comes from the range around the low-binding-energy peak.

There is a problem. The proportionality factor C between the transition rate and the projected DOS in Eq. (8) is difficult to calculate from first principles. We can, however, obtain a consistent value of C if we start from a reasonable assumed value for the target distance, R_{mp}, above only one *particular* lateral position with respect to the surface unit cell. We have done this, and we have also tried several possible values for this assumed value. We find that, provided we do not take too small a value for R_{mp}, our results are not sensitive to the choice. This means that we can predict MIES spectra which do not depend critically on C. Such predictions are, in fact, all that is needed for the interpretation of MIES: the precise value of C would only be a useful observable if some significant fraction of incident helium atoms did not undergo an Auger process, and this is not the case. We shall use the same value of C for both the perfect surface and for that with defects.

Our main choice is based on the value of $R_{\text{mp}}=2.5$ Å for position 1 in Fig. 3a, above the surface oxygen. This choice of R_{mp} was made initially intuitively on the grounds that it seems likely that the value should be slightly larger than an interatomic spacing (since the spacing is related to the ionic radius). We find, in retrospect, that the value also gives the best agreement with the experimental MIES spectrum for the clean MgO(001) surface (see discussion at the end of this section). Given this value, we can estimate C from $\gamma=C/v_0=(\alpha_1/\zeta_1)\exp(\alpha_1 R_{\text{mp}})$ (see Ref. [1]). Note that in all expressions only the combination $\gamma=C/v_0$ is needed, we do not need to know the velocity v_0 by itself. Here, α_1 and ζ_1 are constants fitted to our calculated projected DOS above the oxygen site (position 1). We find $\gamma=3.5921\times10^4$ $\text{Å}^3\,\text{eV}\,\text{s}^{-1}$. With this constant γ, which is the same for any trajectory above both the perfect and the defective surfaces, we can predict the total probability of Eq. (10) for the other positions on the surface including the corresponding R_{mp}, using only quantities which we have calculated: $\Re_p(z)\simeq C\zeta_p\exp(-\alpha_p z)$, where α_p and ζ_p are the corresponding fitting constants for these other positions p. Using this expression, one can calculate the escape probability, Eq. (1), for each lateral position on which the helium atom impinges.

The MIES spectrum is given as follows:

$$P(E_{\text{KE}})=\sum_p w_p P^{(p)}(E_{\text{KE}}) \tag{12}$$

and

$$P^{(p)}(E_{\text{KE}})=\gamma\int_0^\infty D_{1s}^{(p)}(E_{\text{KE}},z)P_{\text{esc}}^{(p)}(z)\,dz. \tag{13}$$

Here, $P_{\text{esc}}^{(p)}(z)\simeq\exp[-\gamma(\zeta_p/\alpha_p)\exp(-\alpha_p z)]$ is the escape probability and $D_{1s}^{(p)}(E,z)$ is the projected DOS for the lateral position p. The integration with respect to z was performed numerically; we used a projected DOS calculated for a mesh of z values between 1 and 4 Å above the surface. In Eq. (12) w_p are the weighting factors corresponding to the lateral positions considered. Since each surface unit cell contains one oxygen atom, one magnesium atom, four side and two centre posi-

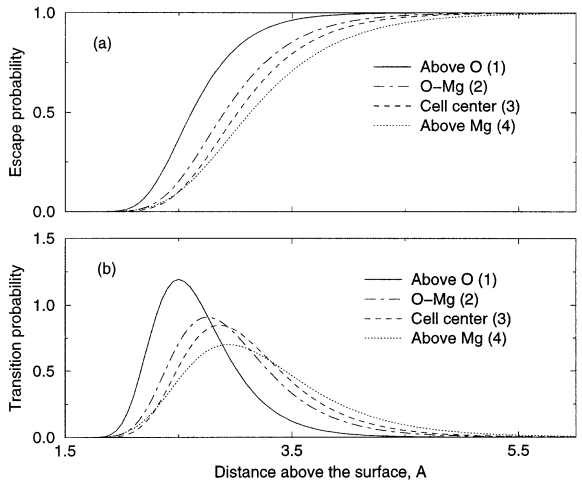

Fig. 6. Escape (a) and transition (b) probabilities for the helium atom above the MgO(001) surface calculated using the assumed most probable target distance of $R_{mp}=2.5$ Å above the oxygen atom.

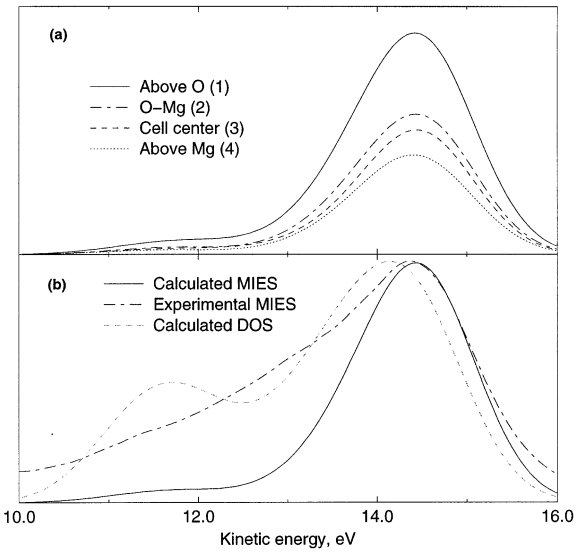

Fig. 7. Calculated contributions to the spectra of emitted electrons from the four positions above the surface primitive unit cell (a), and the calculated final distribution, Eq. (12), surface DOS and the experimental [4] MIES spectra (b). Note that we show kinetic energies, rather than binding energies, so there is a shift equal to the helium excitation energy.

tions, the weights w_p are 1/8, 1/2, 1/4 and 1/8, respectively.

The escape probabilities calculated for the four lateral positions are shown in Fig. 6a. Fig. 6b gives the total transition probability that the helium atom will undergo the Auger transition on the incoming part of its trajectory between $z+\mathrm{d}z$ and z in time interval $\mathrm{d}t=\mathrm{d}z/v_0$ [1]. The total transition probability has been calculated as $P_p(z)\simeq\gamma\zeta_p \exp(-\alpha_p z)P^{(p)}_{esc}(z)$. The transition probability peaks at about 2.5, 2.8, 2.9 and 3.1 Å above the surface for the four lateral positions, respectively (the value of 2.5 Å being our chosen value for above oxygen). The range of distances z for which the Auger transition probability is most effective increases from about 1 Å above oxygen to about 2 Å above magnesium. This reflects the z-dependence of the projected DOS shown in Fig. 5, where the largest inverse decay length was found for helium above oxygen, and the smallest inverse decay length for helium above magnesium. The area under each curve $P_1(z)$, …, $P_4(z)$ is practically equal to unity. This means that practically every helium atom will undergo a transition on the incoming part of its trajectory.

Our calculated transition spectra, $P^{(p)}(E_{KE})$, are shown in Fig. 7a for each lateral position [see Eq. (13)]. To make contact with experiment, we should convert our spectra as a function of binding energy into functions of kinetic energy E_{KE} for the emitted electrons in accordance with Eq. (8). This requires an estimate of the helium atom excitation energy, $E_{He*}-E_{He}$. For consistency, we have calculated this energy, rather than taking the experimental value. We calculated the excitation energy of the helium atom into its lowest triplet state with the Hartree–Fock GAUSSIAN94 code, using the same basis set as in Section 2.3. The energy obtained, 18.7 eV, is marginally smaller than the experimental value of 19.82 eV.

The calculated MIES contributions for each of the four normal trajectories (the four lateral positions) are shown in Fig. 7a. Every predicted MIES curve in Fig. 7a displays a well-defined one-peak structure. The highest intensity is for helium atoms which impinge above the oxygens. This is to be expected, since the valence electrons of the surface which participate in the AD process are localised mostly on oxygen atoms (see, e.g., Ref. [41]).

The final MIES spectra, containing averaging

with respect to the four trajectories and calculated in accordance with Eq. (12), are shown in Fig. 7b. Also shown is the total DOS for the MgO(001) surface, shifted by the 18.7 eV helium excitation energy to allow comparison with electron kinetic energies, as just described. We also show the experimental MIES spectra from Ref. [4]. There are some striking similarities between the curves of Fig. 7b, especially for higher kinetic energies, above about 14 eV. In that region, there is a well-defined peak, and both the position and the slope of the upper-energy side are predicted rather well.

At the low-kinetic-energy side, there are interesting differences. The total surface DOS has a two-peak structure, well known from previous work on the MgO(001) surface (see, e.g., Ref. [41]). Indeed, the experimental UPS spectra reported in Ref. [4] clearly show a two-peak structure which agrees with our calculated surface DOS. However, the calculated MIES spectrum, which is shown in Fig. 7b by the solid line, has only one prominent peak at low binding energies. The single prominent peak agrees with the experimental MIES spectra reported in Ref. [4], also shown in Fig. 7b. The disappearance of the MIES peak at lower kinetic energies (higher binding energies) is due to the faster exponential decay of the orbitals associated with the higher binding energies at those z values at which the AD process has the maximum probability.

However, the predicted MIES peak is significantly narrower than the experimental peak at low kinetic energies. The possible reasons for the discrepancy at low kinetic energies will be discussed in Section 4.

The results we have presented assume that the maximum probability corresponded to a target distance R_{mp} of 2.5 Å above the surface oxygen. To check how this assumption could affect the results, we made similar calculations for both smaller and larger target distances. At smaller distances, such as $R_{mp}=1.5$ Å, we find the contribution of the first DOS peak (low kinetic energy, large binding energy) should be prominent, which contradicts experiment. For larger values, such as $R_{mp}=3.0$ Å, the prediction is essentially the same as for the distance of 2.5 Å.

3.2. Simulation of the MIES spectra for the upright peroxide

A crucial application of an approach like ours is the prediction and possible identification of the signatures of surface defects. We discuss our initial studies of adsorbed atomic oxygen, since this is likely to be created easily. The adsorption of oxygen atoms on the MgO(001) surface has been studied in periodic DFT calculations in Refs. [27–29]. Atomic oxygen sticks to the nearest surface oxygen ion, forming a *peroxy* ion O_2^{2-}. The adsorption energy can be over 2 eV, and depends strongly on the oxygen coordination (plane, terrace, edge or corner). To gain additional Madelung energy, the peroxy ion at the MgO surface is tilted towards another surface oxygen along the [110] direction [27–29]. For CaO(001), however, the upright configuration of the peroxy ion is more favourable energetically, mainly because of the bigger lattice constant [29]. The peroxy ion has an easily recognisable signature in its DOS, corresponding to the formation of a strong chemical bond between the two oxygen atoms. There are three peaks in the DOS: below the O(2p) valence band (VB) due to the bonding O(2pσ) and O(2pπ) orbitals, and the occupied antibonding O(2pπ) state above the O(2p) VB [note that the unoccupied antibonding O(2pσ) state falls within the conduction band]. These features are characteristic both of the upright and tilted configurations of the ion.

The upright configuration of peroxy has higher symmetry, and so is much easier for the projected DOS calculation, since it requires fewer $\boldsymbol{k}$-points. Since we want to focus mainly on the qualitative issues of the peroxy defect signature, we calculated the MIES spectra only for this configuration. We believe that averaging over different defect orientations will not affect our results significantly. We shall not consider in the present paper another possibly significant aspect, namely the effect of the incidence angle of the He^* beam and of the angular distribution of He^* atoms in the beam.

We have used the same slab geometry as for the perfect MgO(001) surface of the previous subsection with the vacuum width equivalent to four atomic layers, but the total number of atoms

has been increased by one oxygen (see Fig. 3b). The relaxed geometry of atoms in the system has been taken from Ref. [28]. Since the symmetry of the system is very high (D_{4h}), only six $\boldsymbol{k}$-points have been used in our projected DOS calculations, which is equivalent to 750 tetrahedra. Likewise, we have considered the same four lateral positions (four trajectories) of the He^* atom as for the perfect surface; we have also included a fifth position (trajectory) above the adsorbed oxygen (see Fig. 3b). The contributions to the spectra have also been calculated in the same way as for the perfect surface, assuming the same factor $\gamma = 3.5921 \times 10^4$ Å^3 eV s^{-1} in the rate expression. As mentioned earlier, this use of the same value of $\gamma = C/v_0$ determines the corresponding R_{mp} for every trajectory for the defective surface.

First, the projected DOS for each of the five positions (trajectories) were calculated at a number of z values above the surface. The preliminary analysis showed that, for positions 2, 3 and 5, it is sufficient to sample the interval 1.75 Å $\leq z \leq$ 5.25 Å, whereas for positions 1 and 4, one must sample the z values between 1 and 5.25 Å. For all cases, the area under the projected DOS, $D_p(z)$, was fitted by a single exponential function, $D_p(z) \simeq \zeta_p \exp(-\alpha_p z)$. Then, both the escape probability, $P_{esc}^{(p)}(z)$, and then the total transition probability, $P_p(z)$, were calculated. Finally, using these data, the transition spectra were integrated over the trajectory of the projectile above each of the five positions.

Fig. 8 shows the total probabilities of the AD process as a function of the distance z from the original MgO surface for all five lateral positions of the helium atom. As expected, above the oxygen ions nearest to the peroxy, and above the surface magnesium ions (positions 1 and 4, respectively), the probabilities are similar to the ones calculated for the perfect surface (cf. Fig. 6b). This means that the He^* atom does not feel the peroxide molecule very much unless it impinges very close to it. The influence of the peroxide is clear for the three other lateral positions. The most probable target distance R_{mp} in position 5 is shifted upwards to 4.75 Å because the adsorbed oxygen sticks out of the surface by 1.4 Å. This value of R_{mp} is 3.35 Å above the adsorbed atom, slightly higher than

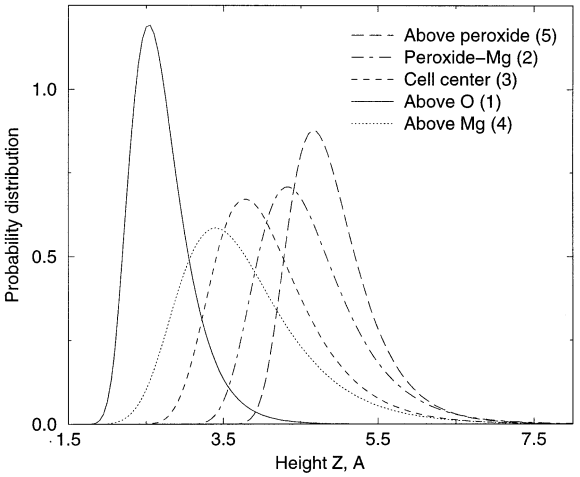

Fig. 8. Calculated transition probabilities for the helium atom above a peroxide molecule at the MgO(001) surface. Numbers in brackets correspond to the position numbers in Fig. 3b.

2.5 Å, the assumed target distance above the oxygen site on the perfect surface. Above positions 2 and 3, which are the closest to the peroxy, the target distance is also higher than above the perfect sites.

The contributions to the MIES spectra for the five positions of the helium atom are shown in Fig. 9. They demonstrate some unexpected fea-

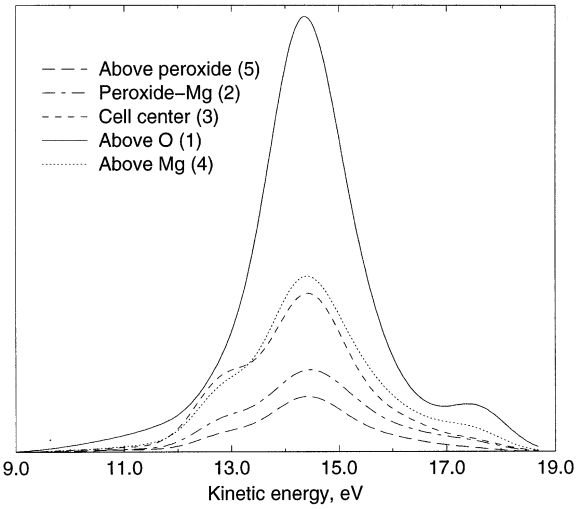

Fig. 9. Calculated contributions to the MIES spectra from the five positions of the He^* atom above the peroxide molecule. Numbers in brackets correspond to Fig. 3b.

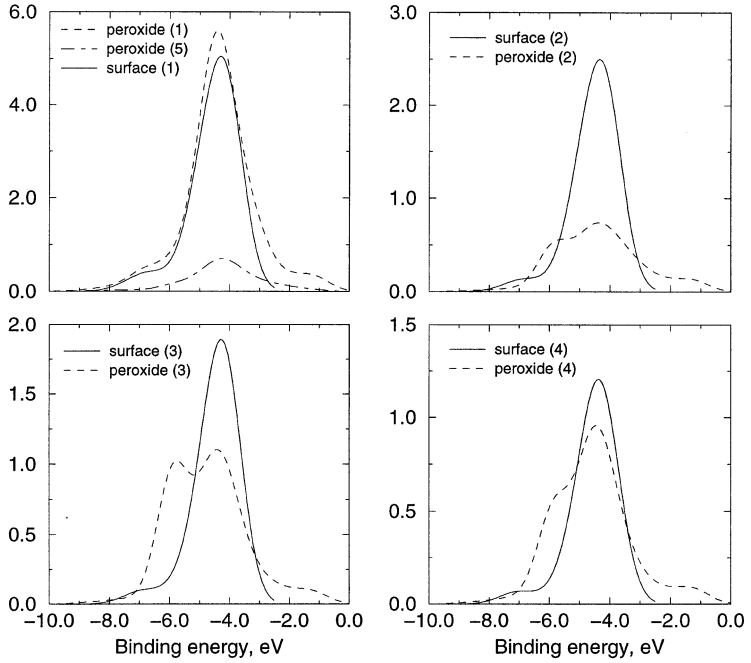

Fig. 10. Calculated projected DOS for the five positions of the He^* atom near the peroxide molecule (marked peroxide) at the most probable target distances (see text). For comparison, similar results are shown for the four positions above the perfect MgO surface, also at the corresponding target distances (marked 'surface'). The positions numbers are shown in brackets. The DOS is shown in arbitrary units, although the absolute values are comparable from one case to another.

tures. First of all, we see that the largest contribution is above the oxygen nearest to the peroxide oxygen atom (position 1). All other contributions, including that from adsorbed oxygen atom, are much smaller. To understand this result, we plot in Fig. 10 the projected DOS above all five positions near the peroxide at the corresponding target distances; namely, 2.5, 4.25, 3.75, 3.5 and 4.75 Å for the positions from 1 to 5, respectively (see Fig. 8). The corresponding projected DOS for the perfect MgO surface above equivalent positions for the corresponding target distances (see Fig. 6b), and in the same units, are also shown for comparison.

The contribution from the peroxy oxygen is very small compared with that of the nearest surface oxygen. The contribution from this nearest oxygen is slightly greater than the contribution from an oxygen on the perfect surface. The contributions at interstitial positions 2 and 3 adjacent to the peroxide system are smaller than those for the equivalent perfect surface sites. The contribution from the magnesium site is largely unaffected by the presence of the peroxy. We can understand the relatively small contribution above the adsorbed oxygen itself by the large target distance (about 4.75 Å with respect to the surface plane), which cuts out most of the contributions from other surface oxygens. Indeed, the target distance is smaller for position 2 and even smaller for position 3, and the projected DOS is significantly increased. On the other hand, the projected DOS for position 1 (above the nearest oxygen to the peroxy) is enhanced with respect to the perfect surface due to the proximity of the adsorbed oxygen atom. Thus, we expect that, on average, the peroxide molecule will reduce the yield in the MIES experiment in the energy region associated with the MgO binding energies, especially at high concentrations of the defect.

Another feature is seen clearly in Figs. 9 and 10 at high kinetic energies, between 16 and 19 eV for

the peroxy ion. These energies are associated with the occupied antibonding O(2pπ) states localised on the peroxy, with binding energies some 0.45 eV above the VB top (see Refs. [27–29]).

In order to calculate the final MIES spectra corresponding to a certain *concentration* of peroxide molecules at the surface, one has to sample the surface area, weighting the various contributions to the spectra, as in Eq. (12). This calculation can be done as follows. Consider a surface area of N primitive unit cells of the perfect surface. There will be exactly N, $4N$, $2N$ and N positions 1, 2, 3 and 4 of the perfect surface. If there is one peroxide molecule in this area, we will have to 'remove' a certain number of the perfect positions around the peroxide and 'substitute' them with the corresponding positions of the defective system. The total MIES spectra will then be given as $P_d(E_{KE}) = P(E_{KE}) + \Delta P_d(E_{KE})$, where $P(E_{KE})$ is the spectrum of the perfect surface and

$$\Delta P_d(E_{KE}) = \frac{c}{8}\left\{\sum_{p=1}^{4}\eta_p[P_d^{(p)}(E_{KE}) - P^{(p)}(E_{KE})] + P_d^{(5)}(E_{KE}) - P^{(1)}(E_{KE})\right\} \quad (14)$$

is the *difference spectrum*. Here $c = 1/N$ is the fractional peroxide concentration, the summation is performed over the first four positions of the helium atom (above oxygen, side, centre and above magnesium), $P_d^{(p)}(E_{KE})$ is the contribution to the spectrum from the given position p of the peroxide system, and η_p is the number of the corresponding positions of the perfect system around the peroxide molecule to be replaced (excluding the oxygen site occupied by the peroxide itself). For $N \geq 8$ the weighting factors η_p do not depend on N (for the first four positions they are all equal to 4) and the difference spectrum appears to be linear with respect to the peroxide concentration. For smaller N these factors depend on N and therefore there is some nonlinearity. If $N = 2$ then $\eta_1 = 1$ and $\eta_4 = 2$; for $N = 4$ and 6 we have $\eta_1 = 2$ and $\eta_4 = 3$; in all these cases $\eta_2 = \eta_3 = 4$.

The calculated total $P(E_{KE})$ and the difference MIES spectra $\Delta P_d(E_{KE})$ for the MgO surface covered with peroxide molecules of different N are shown in Fig. 11. Two effects are evident. First of all, there is a feature at high kinetic energies, above the top of the valence band. This is due to antibonding O(2pπ) states of the peroxide molecule [27,28]. The other two peaks associated with the lower lying binding local states of the peroxide defect do not appear in the MIES spectrum because of the fast decay of their wavefunctions. Secondly, at high peroxide concentrations, amplitudes are reduced in the total spectrum. This is seen in Fig. 11b, and is what one would expect from our previous remarks that surface coverage by oxygen atoms actually reduces the MIES spectra in the energy region associated with the perfect MgO surface.

3.3. Polarisation shift for the peroxide feature

We pointed out in Section 2 that the actual positions of the peaks associated with localised defect states can be shifted by electron relaxation and crystal polarisation associated with the hole produced in the final state. Our estimates show that other terms are negligible; e.g., the polarisation terms (including any image interactions) associated with the helium atom, which is in its ground

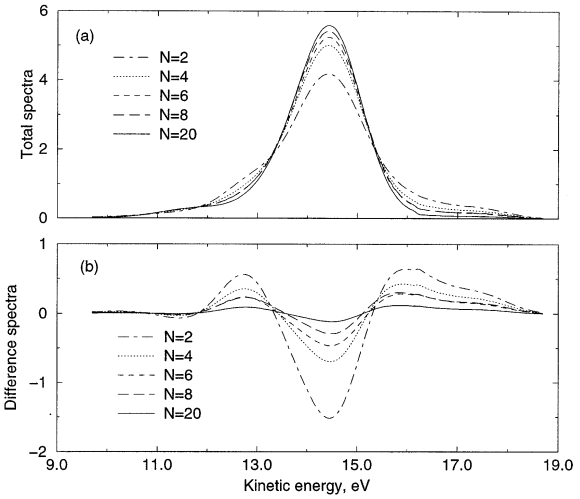

Fig. 11. Calculated total MIES spectra of the emitted electrons (a) and the difference spectra with the perfect surface (b) for the surface containing one peroxide molecule per N primitive surface unit cells. The same (arbitrary) units are used for the intensity.

state. To calculate the final state shift, one has to estimate the energy $W_{\rm pol}^{(k)}$ for the local state ϵ_k associated with the antibonding O(2pπ) peroxy-related state. However, this is difficult, since we are using one-electron Kohn–Sham energies, and it is not clear how to relate them to the total energies in order to calculate this shift [see Eq. (7)]. However, it is still possible to estimate the correct position of the defect-related peak in the MIES spectrum *with respect to* the top of the valence band. Using energy conservation, and combining Eqs. (2) and (3), we obtain for the kinetic energy of an emitted electron:

$$E_{\rm KE} = (E_0 - E_{\rm h}^{(k)}) + (E_{\rm He*} - E_{\rm He}). \quad (15)$$

In DFT the difference of total energies $E_0 - E_{\rm h}^{(k)}$ is the exact *ionisation energy* of the system *if* the state k is the last occupied state [52]. Consider the perfect system first. The largest kinetic energy of the emitted electrons is given by Eq. (15) in which $E_0 - E_{\rm h}^{(k)}$ is the exact ionisation energy of the perfect surface. It is associated with the top of the VB in the MIES spectra. The same consideration for the defective system gives the maximum energy with $E_0 - E_{\rm h}^{(k)}$ being the ionisation energy for the peroxide defect. Since the difference $E_{\rm He*} - E_{\rm He} \simeq 18.7$ eV in our calculations is a constant, the *relative position* of the defect peak in the MIES with respect to the top of the VB in the same spectra will be given as the difference of the ionisation energies of the peroxide and the perfect systems.

In calculating the ionisation energy of the perfect surface, we used several quantum clusters of increasing size, as in Ref. [53]. The hole created after the ionisation of these clusters is delocalised over all cluster oxygens and, for the cluster $Mg_{17}O_5$, we obtained the ionisation energy of 6.86 eV. Then an oxygen atom was added to this cluster, and the geometry of the whole system was optimised, taking into account the lattice polarisation. The O—O distance in the peroxide, the charge distribution and the relaxation of the surface ions obtained in this calculation are close to those obtained in our periodic calculations. The 'vertical' ionisation energy of this system (with only oxygen shells in a region immediately surrounding the cluster allowed to respond) is 6.4 eV. Thus the peroxide state calculated in this way is located about 0.46 eV above the top of the valence band. The hole state appears to be delocalised almost equally among all the oxygen ions in the quantum cluster, including the adsorbed oxygen. The result does not change if we increase the cluster size: both the hole delocalisation and the relative position of the peroxide state with respect to the top of the valence band remain virtually the same. In fact, the energy is very close to the position of the middle of the band of O(2pπ) states obtained in our periodic calculations. Thus, due to the hole delocalisation, the final-state correction in this case is very small.

4. Discussion

In this work we have combined DFT periodic calculations of the surface electronic structure with static perturbation treatment of the Auger de-excitation process. This has enabled us to calculate MIES spectra for the perfect MgO surface and for the surface with an adsorbed oxygen atom.

The interaction between He^* and the surface is treated within first-order perturbation theory, giving the Golden rule formula for the transition rate, Eq. (4). As stressed in the Introduction, this approach needs the interaction between the metastable atom and the surface to be weak. This might not be the case, for the diffuse occupied 2s state of the He^* atom might be affected by the large gradient of the surface electrostatic potential [54]. This would polarise the helium atom, shift the 1s and 2s energies, and curve the He^* trajectories so as to modify the role of the He^* interaction with different surface ions. The surface ions can also be polarised by He^*, although rough estimates suggest this is not important. Since the AD process is non-stationary, it is impossible to consider these effects easily in a static approach. However, we have made some estimates, by treating He^* quantum mechanically, and using pseudopotentials to represent the surface cations and the shell model presentation for the surface oxygens. The results of these calculations show that, in the distance range between He^* and the perfect surface $z \geq 2.5$ Å, there is no significant change of the excitation

energy $E_{He^*} - E_{He}$ of the helium atom. When He^* approaches the adsorbed oxygen atom up to about 3 Å, this energy changes only by 0.3 eV due to the weak Coulomb potential of the peroxide molecule.

Since the polarisability of the surface magnesium ion is much smaller than that of the surface oxygen (which is much larger than that in the bulk [55]), He^* interacts differently with the surface magnesium and oxygen ions. We simulated the possible curving of the He^* trajectories in a classical model taking into account the electrostatic and van der Waals' interactions of He^* with the surface. These calculations have demonstrated that He^* trajectories are likely to deviate significantly from linear trajectory only at beam temperatures less than liquid nitrogen and at very small incidence angles. Based on these results, we believe that our approach is valid for the present experimental conditions.

Comparison of the MIES spectrum calculated for the perfect MgO surface with the experimental one in Fig. 7b demonstrates good qualitative agreement and reproduces the high-kinetic-energy part of the spectrum well. It is this part which is not affected by secondary electrons. Although we did manage to reproduce quite well the experimental one-peak structure of the spectrum (in contrast to the well recognised two-peak structure of the DOS which is very close to the UPS spectrum of MgO [4]), the calculated MIES spectrum appears to be too narrow which results in worse agreement at the low kinetic energies.

Several reasons may affect the comparison of the theoretical and experimental spectra at the low-kinetic-energy part of the spectrum. Our first idea was that the width of the experimental spectrum was broadened by other effects which depend on sample preparation. In particular, one part may be due to secondary electrons enhancing the intensity in the low-kinetic-energy wing of the observed peak. Careful analysis shows that this is unlikely. In the first place, the intensity of the secondaries should not increase with increasing electron energy. Secondly, the MIES spectra are found to be practically identical for differently prepared MgO films and for a single crystal, after subtracting the contribution of the secondary electrons [56]. Another possible reason for the experimental spectrum being too wide might be various impurities, adsorbed species or defects such as steps, kinks, etc. at the surface, which may result in different features at the low-kinetic-energy wing. For example, we have seen in Section 3.2 that, according to our calculations, a peroxide defect produces some feature in this region of the MIES spectrum. Although it is true that real surfaces are rough and contain many defects and adsorbed foreign material, the MIES experiments are performed at high vacuum with a careful control over the purity of the samples used in the experiment [4]. It is very unlikely that there are more than 1% of defects at the MgO surface in the MIES experiments, and these cannot lead to a substantial broadening of the spectra. Note also that there is still no direct experimental evidence for peroxide defects at the MgO surface.

Therefore, it is the theoretical spectrum which appears to be too narrow. We now speculate on possible reasons for this. Several of our approximations and simplifications need to be considered. First of all, the Gaussian smearing of 0.5 eV taken from the earlier work [4] could be significantly underestimated. It corresponds to phonon broadening of the UPS spectra according to the estimates due to Ref. [36]. We have used the same value for the phonon broadening because, in both cases, the initial and final states of the surface are identical. However, different processes are involved in UPS and MIES spectra, so that the broadening may not necessarily be identical. In addition, as has been already mentioned in Section 2.2, other reasons for the smearing also exist which have the effect of using an even wider Gaussian. It is difficult, however, to do any estimates of these effects at the present stage.

We should also mention our assumption concerning the choice of the unknown proportionality factor C between the projected DOS and the transition rate, see Eq. (8) and Section 3.1. The value of C is constrained within sensible limits. Indeed, as has been mentioned at the end of Section 3.1, smaller values of R_{mp} than 2.5 Å for the trajectories which impinge above the oxygens would lead to a wider spectrum due to the reappearance of the second (at high binding energies) peak. This would lead to a rather different struc-

ture of the whole spectrum, and would contradict the experimentally observed one-peak MIES spectrum. We have also tried higher values for R_{mp} (up to 3.5 Å); we find the predictions to be almost identical, although the MIES spectra become slightly narrower due to an effective cut-off of the high-binding-energy side of the first peak. We retain the same value of C/v_0 in all calculations, both for the perfect and the defective surfaces, and this determines the corresponding values of R_{mp} for every trajectory considered.

Another simplification that has been used throughout this work is the assumption of normal trajectories. Lifting this should lead to further broadening of the MIES spectra. To understand this, consider two extreme cases: zero and 90° incidence angles. The latter case corresponds to the normal trajectories considered in this work, where the electrons with high binding energies do not contribute. In the former case, electrons with all binding energies will contribute for the trajectories which are closer than about 2.5 Å to the surface. This should result in some broadening at the low-kinetic-energy wing. At the incidence angle of 45° used in the real experiment, we have an intermediate situation. In addition to that, one has to consider all possible *directions* of the trajectories; for instance, the directions [100] (above both species) and [110] (only above oxygens) will give different spectra and might result in some extra broadening.

We have also made a number of subtle approximations that are difficult to assess fully at the present stage. First of all, the transition rate has been calculated using the projected DOS. Although we believe that this approximation is not significant and we give at least two justifications for it, it may still lead to some change in shape of the theoretical spectra. Additional work is needed to understand the actual consequences of this simplification; we shall do this in the near future. We also mention that we have used DFT wavefunctions in the LDA approximation in the vacuum region some distance (from 1 to 5 Å) away from the surface where the electronic density is very low and changes significantly with the distance. This approximation can also lead to some additional change of the calculated spectrum.

There are no reliable MIES experimental data on adsorbed oxygen atoms on the MgO surface. Three peaks which have been observed in the MIES spectra during oxidation of a magnesium film on the Si(110) substrate in molecular oxygen atmosphere, have been attributed initially to peroxy species at the surfaces [4]. They are absent in the UPS spectra of the same system, which implies that they belong to adsorbed species. These additional peaks had similar character to the surface DOS calculated in Refs. [27–29] for oxygen atom adsorption on the MgO(001) surface: two of them are below the O(2p) VB and one is above it. These data provided one of the reasons for a preliminary assignment. However, a more detailed experimental study reported in Ref. [57] suggests that these peaks should rather be attributed to carbonate formation on the MgO surface. Theory [28,29] also suggests that it is unlikely that oxygen molecules will dissociate to atoms on the perfect MgO surface to form peroxy species. Other processes, such as an interaction of oxygen molecules with the surface F centres, have not been seriously considered. As with most other experimental techniques, one method is often not enough to establish the chemical identity of adsorbed species. The advantage of our theoretical approach is that it not only can predict the MIES spectrum, but also can provide reliable information regarding adsorption energies and diffusion barriers of adsorbed species, which can be correlated, for instance, with temperature-programmed desorption and other spectroscopic data [53].

One may also notice some similarity between MIES and scanning tunnelling microscopy (STM) [58,59] techniques. Both methods give some insight into the structure of the topmost layer of the surface because they are based on electron tunnelling between the crystal surface and a probe. The probe is a metastable atom in the MIES, and a tip in the STM experiment. Another observation is based on our findings concerning the most probable target distances R_{mp} for the peroxide defect. We find that R_{mp} becomes larger in the vicinity of a defect which sticks out of the surface, compared with the value for trajectories which impinge on perfect surface sites. We believe that this is a very general result: one can say that the target distances

follow the topology of the surface in a similar way to that of the tip in STM. Obviously, there are important differences between the two techniques. The STM gives a local geometrical information; the MIES method provides overall electronic structure information about the whole surface of the sample.

Acknowledgements

L.N.K. is supported by EPSRC (grant GR/L02678). P.V.S. would like to thank Kodak for financial support. This work was performed in the framework of a joint collaborative project between University College London and TU Clausthal, Germany, funded by the British Council (grant 887) and DAAD. The authors wish to thank Professor V. Kempter for useful comments on the manuscript and numerous valuable discussions. L.N.K. and A.L.S. thank the members of the entire laboratory for their help and hospitality during their stay in Clausthal. We are grateful to I.V. Abarenkov for useful discussions, and to I. I. Tupitsyn and G. Tsikarishvili for help in calculations.

Appendix A

In this Appendix we show how the projected DOS expression for the AD transition rate used in the main text [see Eq. (8)] can be derived independently. In our analysis we use the first-order perturbation theory to calculate the transition rate. It has been mentioned in the Introduction that, in the case of MIES and oxide surfaces, this method should be valid. Let us consider one He^* atom at the position $\boldsymbol{R}=(x, y, z)$ above the surface. Using Fermi's Golden rule, we write down the transition probability per unit time to emit an electron with momentum $\boldsymbol{Q}$ as:

$$\Re(\boldsymbol{Q})=\frac{2\pi}{\hbar}\sum_{k}^{\mathrm{occ}}|\langle\Psi_{\mathrm{i}}|\hat{H}_{\mathrm{int}}|\Psi_{\mathrm{f}}^{(k\boldsymbol{Q})}\rangle|^2\delta(E_{\mathrm{i}}-E_{\mathrm{f}}^{(k\boldsymbol{Q})}), \tag{A1}$$

where we summed over all events corresponding to all occupied states of the crystal. We do not specify explicitly the interaction operator between the two subsystems, $\hat{H}_{\mathrm{int}}$, which mediates the transition. In the formula above the exact initial state wavefunction of the whole system corresponding to a *non-interacting* He^* atom and the surface is given as

$$\Psi_{\mathrm{i}}(X_N, Y)=\hat{A}[\Psi_0(X_N)\Psi_{\mathrm{He}*}(Y)], \tag{A2}$$

where $\hat{A}$ is the antisymmetrisation operator defined as in Ref. [60], $\Psi_0(X_N)$ is the wavefunction of the surface in the ground singlet state, $X_N=\{x_1, \ldots, x_N\}$ being the coordinates of N surface electrons including spin, $x=(\boldsymbol{r}\sigma)$, and $\Psi_{\mathrm{He}*}(Y)$ is the wavefunction of the He^* atom in the triplet state with both electrons having spin up; $Y=(x_{N+1}, x_{N+2})$ being the corresponding electronic coordinates of the two electrons on the helium atom. The wavefunction of the final state f is then given by

$$\Psi_{\mathrm{f}}^{(k\boldsymbol{Q})}(X_N, Y)=\hat{A}[\Psi_{\mathrm{h}}^{(k)}(X_{N-1})\psi_{\boldsymbol{Q}}(x_N)\Psi_{\mathrm{He}}(Y)], \tag{A3}$$

where $\Psi_{\mathrm{h}}^{(k)}(X_{N-1})$ is the wavefunction of the crystal with one hole in it [$(N-1)$-electron system], i.e. with the state $(k\downarrow)$ destroyed, and the free electron wavefunction, normalised per volume V, is $\psi_{\boldsymbol{Q}}(x)=(1/\sqrt{V})\,\mathrm{e}^{\mathrm{i}\boldsymbol{Q}\boldsymbol{r}}\chi_{\uparrow}(\sigma)$, where $\chi_{\uparrow}(\sigma)$ is the corresponding spin-up function. $\Psi_{\mathrm{He}}(Y)$ is the wavefunction of the ground singlet state of the helium atom.

To simplify the matrix element in Eq. (A1), we use the following approximation which is reminiscent of the well-known Mulliken approximation in semiempirical quantum chemistry [61]:

$$\langle\Psi_{\mathrm{i}}|\hat{H}_{\mathrm{int}}|\Psi_{\mathrm{f}}^{(k\boldsymbol{Q})}\rangle=\frac{1}{2}\,[\langle\Psi_{\mathrm{i}}|\hat{H}_{\mathrm{int}}|\Psi_{\mathrm{i}}\rangle + \langle\Psi_{\mathrm{f}}^{(k\boldsymbol{Q})}|\hat{H}_{\mathrm{int}}|\Psi_{\mathrm{f}}^{(k\boldsymbol{Q})}\rangle]\langle\Psi_{\mathrm{i}}|\Psi_{\mathrm{f}}^{(k\boldsymbol{Q})}\rangle$$

(see also discussion in Ref. [33]). The expression in square brackets above is an average interaction energy between the two systems in the initial and final states, $E_{\mathrm{int}}(\boldsymbol{R})$. Therefore, one approximately

gets:

$$\Re(\boldsymbol{Q}) \simeq \frac{2\pi}{\hbar} E_{\mathrm{int}}(\boldsymbol{R})^2 \sum_{k}^{\mathrm{occ}} |\langle \Psi_{\mathrm{i}} | \Psi_{\mathrm{f}}^{(k\boldsymbol{Q})} \rangle|^2 \delta(E_{\mathrm{i}} - E_{\mathrm{f}}^{(k\boldsymbol{Q})}). \tag{A4}$$

To facilitate the calculation of the overlap integral in the equation above, we first combine the free electron and the crystal hole wavefunctions into one N-electron wavefunction, $\Psi_{\mathrm{h}}^{(k\mathbf{Q})}(X_N) = \hat{A}[\Psi_{\mathrm{h}}^{(k)}(X_{N-1})\psi_{\boldsymbol{Q}}(x_N)]$, so that the integral to calculate becomes:

$$\langle \Psi_{\mathrm{i}} | \Psi_{\mathrm{f}}^{(k\boldsymbol{Q})} \rangle = \langle \Psi_0(X_N) \Psi_{\mathrm{He}*}(Y) | \hat{A} \times [\Psi_{\mathrm{h}}^{(k\boldsymbol{Q})}(X_N) \Psi_{\mathrm{He}}(Y)] \rangle \tag{A5}$$

(see, e.g., Ref. [60]). This type of overlap integral is met in the *Theory of Electronic Separability* [60]. Indeed, we have two electronic groups here: one containing N electrons, and another one, containing only two electrons. The wavefunctions of the two electronic groups cannot be treated as being strongly orthogonal (see, e.g., Ref. [60]), however, as we are interested in their overlap. The *Arrow Diagram* method developed in Refs. [62,63] appears to be an ideal mathematical tool in this case. Since there are only two electronic groups, one of which contains only two electrons, we have only three diagrams to consider as are shown in Fig. A1.

The first (trivial) diagram contains no permutation and therefore does not give any contribution to the overlap integral due to orthogonality of the helium wavefunctions $\Psi_{\mathrm{He}*}$ and Ψ_{He} corresponding to different spin states of the atom. The second diagram contains one permutation whereas the third diagram contains two permutations between the helium and the crystal wavefunctions. It is sufficient to use the second diagram only as the third diagram is of the next order with respect to overlap and will be neglected here. This is well justified as the overlap between the wavefunctions of the surface electrons and the helium atom is extremely small at the distances where the transition happens. Therefore, keeping only the contribution from the first diagram and using the general rules formulated in Ref. [63], we have:

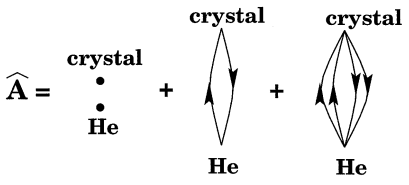

Fig. A1. Arrow diagrams between the helium atom and the crystal used in the calculation of the overlap integral in Eq. (A5).

$$\langle \Psi_{\mathrm{i}} | \Psi_{\mathrm{f}}^{(k\boldsymbol{Q})} \rangle = -\int \rho(x; x'|0; h(k\boldsymbol{Q})) \times \rho(x'; x|\mathrm{He}^*; \mathrm{He})\, \mathrm{d}x\, \mathrm{d}x', \tag{A6}$$

where we introduced two transition density matrices [60] of the first order, defined as:

$$\rho(x; x'|0; h(k\boldsymbol{Q})) = N \int \Psi_0(x, X')^* \Psi_{\mathrm{h}}^{(k\boldsymbol{Q})}(x', X')\, \mathrm{d}X' \tag{A7}$$

and

$$\rho(x; x'|\mathrm{He}^*; \mathrm{He}) = 2 \int \Psi_{\mathrm{He}*}(x, x_2)^* \Psi_{\mathrm{He}}(x', x_2)\, \mathrm{d}x_2, \tag{A8}$$

and $X' = (x_2, \ldots, x_N)$.

The integral in Eq. (A6) is not easy to calculate in the general case. In the one-electron approximation $\rho(x; x'|0; h(k\boldsymbol{Q})) = \psi_{k\downarrow}(x)^* \psi_{\boldsymbol{Q}\uparrow}(x')$ and $\rho(x'; x|\mathrm{He}^*; \mathrm{He}) = \psi_{2\mathrm{s},\uparrow}(x')^* \psi_{1\mathrm{s},\downarrow}(x)$ (see, e.g., Ref. [60]). Using these expressions in Eq. (A6) and performing spin integrations, we finally have $\langle \Psi_{\mathrm{i}} | \Psi_{\mathrm{f}}^{(k\mathbf{Q})} \rangle = \langle \psi_{2\mathrm{s}} | \psi_{\boldsymbol{Q}} \rangle \langle \psi_k | \psi_{1\mathrm{s}} \rangle$ which allows us to represent the transition rate of Eq. (A4) as

$$\Re(\boldsymbol{Q}) = \frac{2\pi}{\hbar} E_{\mathrm{int}}(\boldsymbol{R})^2 |\langle \psi_{2\mathrm{s}} | \psi_{\boldsymbol{Q}} \rangle|^2 \left[\sum_{k}^{\mathrm{occ}} |\langle \psi_k | \psi_{1\mathrm{s}} \rangle|^2 \delta(E_{\mathrm{i}} - E_{\mathrm{f}}^{(k\boldsymbol{Q})}) \right].$$

Note that since the overlap integral $\langle \psi_{2\mathrm{s}} | \psi_{\boldsymbol{Q}} \rangle \propto \mathrm{e}^{\mathrm{i}\boldsymbol{Q}\boldsymbol{R}}$, the position $\boldsymbol{R}$ of the helium atom disappears from its module. Therefore, the $\boldsymbol{R}$-dependence comes from the interaction energy, $E_{\mathrm{int}}(\boldsymbol{R})$, and the overlap integrals $\langle \psi_k | \psi_{1\mathrm{s}} \rangle$ between the surface electrons and the 1s helium orbital.

Note also that the integral $\langle\psi_{2s}|\psi_{\boldsymbol{Q}}\rangle$ does not depend on the *direction* of the momentum $\boldsymbol{Q}$; it does, however, depend on $|\boldsymbol{Q}|$ and therefore on the energy E_{KE} of the emitted electron — this dependence is rather weak due to plane-wave character of the free electron orbital. If we neglect this dependence and also the dependence of $E_{\mathrm{int}}(\boldsymbol{R})$ on $\boldsymbol{R}$, then Eq. (6) of the main text is recovered.

Note that the same result is obtained also for other metastables containing more than two electrons (like Ar^*, for example) although the meaning of the orbitals denoted ψ_{1s} and ψ_{2s} above will be different. Indeed, in these cases we have additional diagrams to those shown in Fig. A1 which contain three, four, etc. number of permutations. These diagrams lead to higher-order contributions to the overlap integral and therefore can be neglected.

References

[1] H.D. Hagstrum, Phys. Rev. 96 (1954) 336.
[2] Y. Harada, S. Masuda, H. Ozaki, Chem. Rev. 97 (1997) 1897.
[3] V. Kempter, Mater. Sci. Forum 239–241 (1997) 621.
[4] D. Ochs, W. Maus-Friedrichs, M. Brause, J. Günster, V. Kempter, V. Puchin, A.L. Shluger, L.N. Kantorovich, Surf. Sci. 365 (1996) 557.
[5] B. Heinz, H. Morgner, Surf. Sci. 405 (1998) 104.
[6] V.E. Puchin, J.D. Gale, A.L. Shluger, E.A. Kotomin, J. Günster, M. Brause, V. Kempter, Surf. Sci. 370 (1997) 190.
[7] P. Fouquet, P.K. Day, G. Witte, Surf. Sci. 400 (1998) 140.
[8] A. Zwartkruis, T. Fondén, Surf. Sci. 269 (1992) 601.
[9] A. Zwartkruis, T. Fondén, Phys. Rev. B 48 (1993) 15603.
[10] M. Alducin, F.J. García de Abajo, P.M. Echenique, Phys. Rev. B 49 (1994) 14589.
[11] M.A. Cazalilla, N. Lorente, R. Díz Muiño, J.-P. Gauyacq, D. Teillet-Billy, P.M. Echenique, Phys. Rev. B 58 (1998) 13991.
[12] R. Hentschke, K.J. Snowdon, P. Hertel, W. Heiland, Surf. Sci. 173 (1986) 565.
[13] J.A. Appelbaum, D.R. Hamann, Phys. Rev. B 12 (1975) 5590.
[14] Z.L. Mišković, R.K. Janev, Surf. Sci. 166 (1986) 480.
[15] Z.L. Mišković, R.K. Janev, Surf. Sci. 221 (1989) 317.
[16] A.T. Amos, K.W. Sulston, S.G. Davison, Adv. Chem. Phys. 76 (1989) 335.
[17] B.L. Burrows, A.T. Amos, Z.L. Miŝković, S.G. Davison, Phys. Rev. B 51 (1995) 1409.
[18] K. Makoshi, Surf. Sci. 254 (1991) 281.
[19] K. Makoshi, H. Kaji, Progr. Theor. Phys. Suppl. 106 (1991) 327.
[20] L.V. Keldysh, Sov. Phys. — JETP 20 (1965) 1018.
[21] C.A. Moyer, K. Orvek, Surf. Sci. 114 (1982) 295.
[22] C.A. Moyer, K. Orvek, Surf. Sci. 121 (1982) 138.
[23] D. Ochs, M. Brause, P. Stracke, S. Krischok, F. Wiegershaus, W. Maus-Friedrichs, V. Kempter, V.E. Puchin, A.L. Shluger, Surf. Sci. 383 (1997) 162.
[24] C. Pisani, R. Dovesi, C. Roetti, in: Hartree–Fock Ab Initio Treatment of Crystalline Systems, Lecture Notes in Chemistry, vol. 48, Springer, Berlin, 1988.
[25] R. Dovesi, V.R. Saunders, C. Roetti, M. Causa, N.M. Harrison, R. Orlando, E. Apra, CRYSTAL95 User's Manual, University of Torino, Torino, 1996.
[26] L.J. Clarke, I. Stich, M.C. Payne, Comp. Phys. Commun. 72 (1992) 14.
[27] L.N. Kantorovich, M.J. Gillan, J.A. White, J. Chem. Soc., Faraday Trans. 92 (1996) 2075.
[28] L.N. Kantorovich, M.J. Gillan, Surf. Sci. 374 (1997) 373.
[29] L.N. Kantorovich, M.J. Gillan, Mater. Sci. Forum 239–241 (1997) 637.
[30] P.A. Zeijlmans van Emmichoven, P.A.A.F. Wouters, A. Niehaus, Surf. Sci. 195 (1988) 115.
[31] P. Eeken, J.M. Fluit, A. Niehaus, I. Urazgil'din, Surf. Sci. 273 (1992) 160.
[32] L.N. Kantorovich, P.B. Zapol, Phys. Stat. Sol. (b) 183 (1994) 201.
[33] A.M. Stoneham, Theory of Defects in Solids, Clarendon, Oxford, 1975.
[34] J.J. Markham, Rev. Mod. Phys. 31 (1959) 956.
[35] G.D. Mahan, Phys. Rev. B 21 (1980) 4791.
[36] M. Iwan, C. Kunz, Phys. Lett. A 60 (1977) 345.
[37] M.C. Payne, M.P. Teter, D.C. Allan, T.A. Arias, J.D. Joannopoulos, Rev. Mod. Phys. 64 (1992) 1045.
[38] M.J. Gillan, L.N. Kantorovich, P.J.D. Lindan, Curr. Opin. Solid State Mater. Sci. 1 (1996) 820.
[39] A.L. Shluger, P.V. Sushko, L.N. Kantorovich, Phys. Rev. B 59 (1999) 2417.
[40] A.L. Shluger, L.N. Kantorovich, A.I. Livshits, M.J. Gillan, Phys. Rev. B 56 (1997) 15332.
[41] L.N. Kantorovich, J. Holender, M.J. Gillan, Surf. Sci. 343 (1995) 221.
[42] A.L. Shluger, A.L. Rohl, D.H. Gay, R.T. Williams, J. Phys.: Condens. Matter 6 (1994) 1825.
[43] B.G. Dick, A.W. Overhauser, Phys. Rev. 112 (1958) 603.
[44] G.W. Trucks, H.B. Schlegel, P.M.W. Gill, B.G. Johnson, M.A. Robb, J.R. Cheeseman, T.A. Keith, G.A. Petersson, J.A. Montgomery, K. Raghavachari, M.A. Al-Laham, V.G. Zakrzewski, J.V. Ortiz, J.B. Foresman, J. Cioslowski, B.B. Stefanov, A. Nanayakkara, M. Challacombe, C.Y. Peng, P.Y. Ayala, W. Chen, M.W. Wong, J.L. Andres, E.S. Replonge, R. Gomperts, R.L. Martin, D.J. Fox, J.S Binkley, D.J. Defrees, J. Baker, J.P. Stewart, M. Head-Gordon, C. Gonzalez, J.A. Pople, GAUSSIAN94 (Revision E.1), Gaussian Inc, Pittsburgh, PA, 1995.
[45] A.D. Becke, J. Chem. Phys. 98 (1993) 5648.
[46] W.J. Hehre, R. Ditchfield, J.A. Pople, J. Chem. Phys. 56 (1972) 2257.
[47] W.R. Wadt, P.J. Hay, J. Chem. Phys. 82 (1985) 284.

[48] D.M. Ceperley, B.J. Alder, Phys. Rev. Lett. 45 (1980) 566.
[49] L.N. Kantorovich, unpublished.
[50] R.G. Newton, Quantun Theory of Scattering, McGraw-Hill, New York, 1966.
[51] A. Zangwill, Physics at Surfaces, Cambridge University Press, Cambridge, 1996.
[52] R.O. Jones, O. Gunnarsson, Rev. Mod. Phys. 61 (1989) 689.
[53] L.N. Kantorovich, A.L. Shluger, P.V. Sushko, A.M. Stoneham, J. Günster, P. Stracke, D.M. Goodman, V. Kempter, Faraday Discuss. 114 (1999) in press.
[54] S. Ustaze, R. Verucchi, S. Lacombe, L. Guillemot, V.A. Esaulov, Phys. Rev. Lett. 79 (1997) 3526.
[55] P.W. Fowler, P. Tole, Surf. Sci. 197 (1988) 457.
[56] V. Kempter, private communication.
[57] D. Ochs, M. Brause, B. Braun, W. Maus-Friedrichs, V. Kempter, Surf. Sci. 397 (1998) 101.
[58] G. Binnig, H. Rohrer, Ch. Gerber, E. Werbel, Phys. Rev. Lett. 49 (1982) 57.
[59] G. Binnig, H. Rohrer, Rev. Mod. Phys. 59 (1987) 615.
[60] R. McWeeny, Methods of Molecular Quantum Mechanics, Academic Press, London, 1992.
[61] R.S. Mulliken, J. Chem. Phys. 49 (1949) 497.
[62] L.N. Kantorovich, B.P. Zapol, J. Chem. Phys. 96 (1992) 8420.
[63] L.N. Kantorovich, B.P. Zapol, J. Chem. Phys. 96 (1992) 8427.